arXiv:1612.07196v1 [cond-mat.quant-gas] 21 Dec 2016

Observation of interspecies Feshbach resonances in an ultracold ^{39}K-^{133}Cs mixture and refinement of interaction potentials

Michael Gröbner,[1] Philipp Weinmann,[2] Emil Kirilov,[1] Hanns-Christoph Nägerl,[1] Paul S. Julienne,[3] C. Ruth Le Sueur,[4] and Jeremy M. Hutson[4]

[1]*Institut für Experimentalphysik und Zentrum für Quantenphysik, Universität Innsbruck, 6020 Innsbruck, Austria*
[2]*Institut für Quantenoptik und Quanteninformation (IQOQI), Österreichische Akademie der Wissenschaften, 6020 Innsbruck, Austria*
[3]*Joint Quantum Institute, University of Maryland and National Institute for Standards and Technology, College Park, Maryland 20742, U.S.A.*
[4]*Joint Quantum Centre (JQC) Durham-Newcastle, Department of Chemistry, Durham University, South Road, Durham, DH1 3LE, United Kingdom*

We observe interspecies Feshbach resonances due to s-wave bound states in ultracold ^{39}K-^{133}Cs scattering for three different spin mixtures. The resonances are observed as joint atom loss and heating of the K sample. We perform least-squares fits to obtain improved K-Cs interaction potentials that reproduce the observed resonances, and carry out coupled-channel calculations to characterize the scattering and bound-state properties for ^{39}K-Cs, ^{40}K-Cs and ^{41}K-Cs. Our results open up the possibilities of tuning interactions in K-Cs atomic mixtures and of producing ultracold KCs molecules.

PACS numbers: 34.50.Cx, 34.20.Cf, 67.60.Bc

I. INTRODUCTION

The possibility of controlling collisional interactions in ultracold atomic samples to very high precision through Feshbach resonances [1] is the foundation of many different cold atom experiments. Control of interactions by Feshbach tuning has enabled experiments e.g. on tunable quantum gases [2–4], the creation of ultracold Feshbach molecules [5–7], the formation of Bose-Einstein condensates (BECs) of molecules [8, 9] and the observation of the BEC-BCS crossover [10–12], few-body and Efimov physics [13], polaron physics [14, 15], and novel states, phase transitions, and dynamics in one-dimensional gases [16–18]. In these experiments, intraspecies interactions were tuned, in some cases between different spin states of the same species. In recent years, interest has turned to mixtures of quantum gases and the tuning of interspecies interactions. This interest is motivated by the study of exotic phases such as supersolids [19], the heteronuclear Efimov scenario for a three-body system [20–22], boson-mediated superfluids [23], quantum phases that involve composite fermions [24], mixtures under simultaneous superfluidity [25], and the possibility of forming samples of ultracold polar ground-state molecules [26]. In particular, the electric dipole moment of heteronuclear molecules gives rise to anisotropic, long-range dipole-dipole interactions that contrast with the isotropic, short-range interaction in atomic experiments [27, 28]. Combining long-range interactions with optical lattice potentials allows the study of exotic quantum phases such as pair superfluids and the implementation of quantum simulation and quantum information processing [29–32].

Experimentally, systems of ultracold ground-state molecules are produced in a two-step procedure: First, atoms in nearly quantum-degenerate atomic mixtures are magneto-associated using a Feshbach resonance to form weakly bound molecules. Second, these molecules are optically transferred into the rovibrational ground state by stimulated Raman adiabatic passage (STIRAP) [33–35]. This procedure, which requires precise knowledge of the inter- and intraspecies scattering properties, has recently led to the production of ultracold and dense samples of heteronuclear molecules such as fermionic KRb [26] and NaK [36] and bosonic RbCs [37–39] and NaRb [40] in their rovibrational ground states. The present paper is aimed towards the goal of producing ultracold KCs molecules by similar methods. Ground-state KCs molecules are of particular interest because of their large electric dipole moment (1.92 D) [41] and their stability under two-body molecular collisions [42], which makes ^{40}KCs the only chemically stable fermionic alkali dimer apart from Na^{40}K. Additionally, the two available bosonic isotopes ^{39,41}K increase the flexibility in mixing and dimer association with Cs.

In most magneto-association experiments so far, molecules were produced in 3D bulk atom mixtures [26, 36–38, 40]. Only a comparatively small fraction of atoms could be converted to heteronuclear dimers, because in bulk samples the process is limited by atomic three-body recombination and vibrational relaxation in atom-molecule and molecule-molecule collisions. Such losses can be suppressed if the two atomic samples are overlapped in an optical lattice, creating either a Bose/Fermi Mott insulator/band insulator [43] or a Bose/Bose double-species Mott insulator [39]. In both cases reported so far, a Feshbach resonance was exploited in two different ways. First, it was used to null the interspecies interaction at the zero-crossing of the resonance to achieve efficient sample mixing. Subsequently, the resonance was used to form the molecules from atom pairs. Lattice filling fractions of 30% and above have been achieved. Since we aim at a similar strategy for KCs, precise knowledge of the Feshbach resonance positions and widths is crucial.

The individual two-body interaction properties of ^{39}K [44] and Cs [45, 46] are well understood. This has allowed the production of Bose-Einstein condensates for each species separately [47–50] and for both species in the same apparatus [51]. The singlet and triplet interaction potentials for KCs

have been determined from extensive electronic spectroscopy by Ferber *et al.* [52, 53]; in the present work we designate the potentials of Ref. [53] the F2013 potentials. Patel *et al.* [54] have carried out coupled-channel calculations on the F2013 potentials to obtain the positions and widths of Feshbach resonances for all three K isotopes, including both s-wave and d-wave bound states. However, no experiments have yet been carried out to test these predictions. In this article, we report the observation of Feshbach resonances in an ultracold ^{39}K-^{133}Cs mixture. We prepare the samples in different spin states and search for loss features as we scan the homogeneous magnetic field in the range from 0 G to 650 G. The observed resonances in the lowest spin state are observed at magnetic fields about 20 G higher than predicted in Refs. [53] and [54]. We therefore use coupled-channel calculations to assign the resonances and to fit improved interaction potentials, which we designate G2017. We then use the new potentials to make improved predictions of resonance positions and widths for all three isotopologs of KCs.

II. EXPERIMENT

Techniques for the preparation of ultracold Cs [55] and ^{39}K [51, 56] are well established, but mixing the two species is not straightforward. In particular, mixing the samples in the regime of quantum degeneracy is quite involved and we are presently attempting a strategy similar to that demonstrated for ^{87}RbCs in Ref. [39]. For the present goal of detecting interspecies Feshbach resonances, however, it is sufficient to mix very cold thermal samples, and even that poses some challenges. The different steps in laser cooling lead to a disparity in the sample temperatures ($\geq 5\ \mu$K for ^{39}K and $\leq 1\ \mu$K for Cs) and densities. The Ramsauer-Townsend minimum for ^{39}K at $\sim 400\ \mu$K [57], the large losses when ^{39}K atoms overlap with the Cs magneto-optical trap (MOT), and the strong heating when Cs is loaded into a deep dipole trap make a sequential cooling scheme necessary. We achieve this with a translatable and transformable trap. Specifically, we first load the ^{39}K sample into a very tight optical trap, subsequently translate this sample vertically to allow for Cs loading and cooling, and finally bring the two species together in a relaxed trap with enlarged waist that is suitable for both species.

The experimental sequence starts with the preparation of an ultracold K sample as described in Ref. [51]. In short, after standard laser cooling and spin polarizing on the D_2 and D_1 lines, we load up to 5×10^8 atoms in the $|\mathrm{K:c}\rangle \equiv |f=1, m_f=-1\rangle$ hyperfine Zeeman sublevel into a magnetic quadrupole trap. To overcome the Ramsauer-Townsend scattering minimum caused by the negative background scattering length, we superimpose a dipole trap beam with $1/e^2$-waist of 26 μm at 1064 nm and an initial power of 15 W, and simultaneously increase the quadrupole field within 5 s from 32 G/cm to 75 G/cm (along the coil axis). Although this increases the temperature, the higher density ensures efficient loading of the tight tweezer trap. The quadrupole field is shut off and the magnetic offset field B is then ramped to 42.5 G. At this field the scattering length for atoms in state $|\mathrm{K:c}\rangle$ is around $100\,a_0$

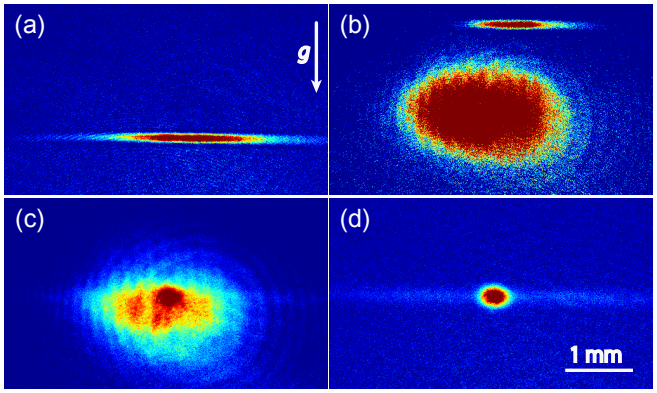

FIG. 1: Experimental sequence to combine ^{39}K with ^{133}Cs as shown in absorption images. (a) In-situ image of the K sample after dipole trap loading. (b) Vertically displaced K cloud (upper cloud) to avoid collisional loss with Cs atoms (lower cloud) during Cs laser cooling. (c) Merged samples at the end of the Cs MOT stage. The K sample shows up as the dark red disk at the center of the image. (d) Typical K signal in the crossed trap for a K-Cs mixture after merging. The images in (b) and (c) are overlapped absorption images taken at the respective imaging wavelengths.

and we can perform efficient forced evaporative cooling. For this, the power of the single-beam dipole trap is decreased exponentially in 1.5 s to 150 mW. During the first 600 ms of this ramp we move the optical trap 1.2 mm upwards (see Fig. 1(a-b)). The vertical transport is achieved by moving a lens and a mirror that are mounted on a motorized translation stage and works without any observable atom loss or heating. We note that magnetization effects related to our stainless steel vacuum chamber require a magnetic polarization stage after the quadrupole trap. Polarization is achieved by pulsing B several times up to 1000 G for 100 ms. Without this procedure, laser cooling of Cs, as performed subsequently, is not possible without adjustments in the magnetic field.

At this point, the magnetic trap center is free and we can start loading the Cs MOT. For this, we turn the quadrupole field on again (7.5 G/cm along the coil axis). During the first 100 ms we linearly increase the K trap power to 300 mW and turn on a 15-W dipole trap beam with a waist of 250 μm at $\sim$1070 nm, crossing the center of the Cs MOT. After 5 s of Cs MOT loading, and before increasing the quadrupole field to 20 G/cm to compress the Cs sample, we superimpose the two clouds (see Fig. 1(c)). This is done by moving the K trap 0.79 mm downwards in 160 ms. At the same time we dynamically increase the waist of the K trap from 26 μm to 63 μm by shrinking the aperture of an iris with a servomotor and increase the power to 1.2 W. After the compression stage the Cs sample is further cooled and spin-polarized by three-dimensional degenerate Raman-sideband cooling (dRSC) [58, 59]. The temperature after dRSC is below 1 μK when we release the atoms into free space. Here, however, we cool the atoms into a crossed-dipole trap. When we do so, we measure temperatures of about 7 μK and observe some significant atom loss. We attribute the tempera-

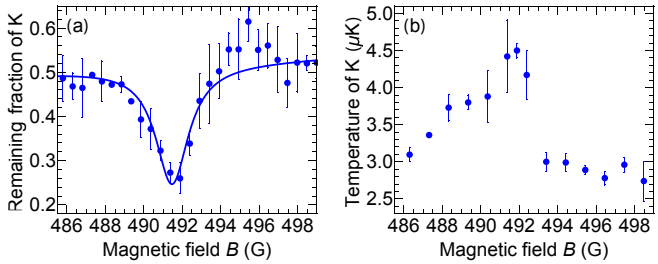

FIG. 2: Typical Feshbach resonance signatures in a $|\mathrm{K:c}\rangle$-$|\mathrm{Cs:a}\rangle$ mixture. (a) Normalized atom number and (b) temperature for a K sample mixed with Cs after a 900 ms hold time. (a) The remaining fraction of K atoms normalized to a sample without Cs at constant trap depth after a hold time of 100 ms. Each point is an average of at least two measurements and the solid line is a Lorentzian fit to the results. The temperatures in (b) are deduced from 5 time-of-flight images with different expansion times and the error bars represent statistical errors from the temperature fits. Larger data samples were not possible due to drifts of the vacuum chamber magnetization as discussed in the text.

TABLE I: Overview of interspecies Feshbach resonances for mixtures $|\mathrm{K:a}\rangle$-$|\mathrm{Cs:a}\rangle$, $|\mathrm{K:b}\rangle$-$|\mathrm{Cs:a}\rangle$, and $|\mathrm{K:c}\rangle$-$|\mathrm{Cs:a}\rangle$. Experimentally we deduce the positions B_0 and FWHM δ by fitting Lorentzian functions to the loss features. The uncertainties are the statistical errors from the Lorentzian fits. Note that the Lorentzian width δ is not the same physical quantity as the theoretical width Δ. We note that drifts of the chamber magnetization result in a systematic error of up to 0.3 G for B_0.

	Experiment		Theory (F2013 potentials)	
Spin states	B_0 (G)	δ (G)	B_0 (G)	Δ (G)
$\|\mathrm{K:a}\rangle$+ $\|\mathrm{Cs:a}\rangle$	361.1(1)	3.2(4)	341.89	4.7
	442.59(1)	0.28(3)	421.37	0.38
$\|\mathrm{K:b}\rangle$+ $\|\mathrm{Cs:a}\rangle$	419.3(1)	3.0(5)	399.93	4.3
	513.12(1)	0.16(6)	491.39	0.55
$\|\mathrm{K:c}\rangle$+ $\|\mathrm{Cs:a}\rangle$	491.5(1)	2.1(4)	471.97	3.8
	599.32(3)	0.5(1)	575.67	0.44

ture increase and atom loss largely to the mismatch of the Cs cloud size after dRSC to the trapping volume of the crossed-dipole trap and possibly to ac-Stark shifts due to the dipole trap that compromise the performance of dRSC. Also, atoms that are cooled away from the center of the crossed-dipole trap convert potential energy into kinetic energy after extinction of the dRSC lattice beams. In any case, after a hold time of 80 ms at 35.5 G in the crossed-dipole trap, the K and Cs clouds (see Fig. 1(d)) are each found to be in thermal equilibrium, but at different temperatures. They see trap depths of about $U_\mathrm{K}/k_\mathrm{B} = 20\ \mu$K and $U_\mathrm{Cs}/k_\mathrm{B} = 39\ \mu$K. With around 1×10^5 K atoms and 1×10^5 Cs atoms in the trap, we measure temperatures of $T_\mathrm{K} = 3\ \mu$K and $T_\mathrm{Cs} = 7\ \mu$K. We measure trap frequencies of $\omega_\mathrm{K}/2\pi = (374, 84, 383)$ Hz and $\omega_\mathrm{Cs}/2\pi = (281, 63, 288)$ Hz and deduce atomic peak densities of $n_\mathrm{K} = 1.2\times10^{12}$ cm^{-3} and $n_\mathrm{Cs} = 9\times10^{11}$ cm^{-3}. At this stage, the K atoms are fully spin polarized in the third-lowest energy state $|\mathrm{K:c}\rangle$. The Cs atoms are 80% polarized in the $|\mathrm{Cs:a}\rangle \equiv |f=3, m_f=3\rangle$ state, with the rest of the Cs sample mainly populating the $|\mathrm{Cs:b}\rangle \equiv |f=3, m_f=2\rangle$ state.

The dipole trap now allows us to prepare K-Cs mixtures in any desired hyperfine state combination. Here, to provide sufficient input to theoretical modeling, we are mainly interested in combining $|\mathrm{Cs:a}\rangle$ with $|\mathrm{K:a}\rangle \equiv |f=1, m_f=1\rangle$, $|\mathrm{K:b}\rangle \equiv |f=1, m_f=0\rangle$, and $|\mathrm{K:c}\rangle$. We fully spin-polarize the Cs sample into the $|\mathrm{Cs:a}\rangle$ state by using a microwave pulse in combination with resonant light to clean out the $|\mathrm{Cs:b}\rangle$ population. During the pulse, which lasts 6 ms and is resonant with the transition from $|\mathrm{Cs:b}\rangle$ to $|f=4\rangle$, we sweep B from 1 G to 1.05 G to address magnetic field inhomogeneities, and apply laser light on the $6^2\mathrm{S}_{1/2}\ |f=4\rangle \rightarrow 6^2\mathrm{P}_{3/2}|f'=5\rangle$ transition.

First, we perform Feshbach spectroscopy on a $|\mathrm{K:c}\rangle$-$|\mathrm{Cs:a}\rangle$ mixture. For this, we linearly ramp the magnetic offset field B within 10 ms to any desired value in the range from 0 G to 650 G and hold it there for 900 ms to 1300 ms. During this hold time we exponentially decrease the power of the transformable beam to 520 mW in order to enhance the loss of K atoms from the crossed trap. In the vicinity of an interspecies Feshbach resonance, the K sample undergoes enhanced trap loss through three-body recombination and heating from the interaction with the hotter Cs sample. To detect the remaining fraction of K atoms we ramp B within 10 ms to 0.1 G before applying standard absorption imaging. For this particular spin mixture we scan B in 1-G steps from 0 G to 650 G and observe two loss features, one broad and one narrow, located around 491.5 G and 599.3 G, respectively. We scan the loss features with finer resolution in B. The loss occurs over a range of 0.1 to several G, depending on the resonance and the specific experimental conditions. The results around 491.5 G are shown in Fig. 2(a). The K atom number shows a clear loss maximum. The loss minimum that appears around 495.5 G may be the result of the zero-crossing of the scattering length on the high-field side of the resonance. We fit Lorentzian functions to the loss features to obtain the positions of maximum loss B_0 and the full widths at half maximum (FWHM) δ.

We also carry out time-of-flight measurements to determine the temperature of the K sample. The results are shown in Fig. 2(b); we observe an increase in temperature from 3.0 μK to 4.5 μK at the same location as the loss is maximal. This temperature increase vanishes when the Cs sample is absent. We attribute the increase in temperature to partial thermalization with the hotter Cs sample. Higher temperatures are probably counteracted by evaporation due to the finite trap depth. As will be seen in section III D below, the background scattering length for ^{39}K-Cs is around 70 a_0, and this relatively small value explains the absence of observed thermalization away from resonance.

For Feshbach spectroscopy with K atoms in $|\mathrm{K:b}\rangle$ and $|\mathrm{K:a}\rangle$ we transfer the K atoms by radio-frequency adiabatic passage from $|\mathrm{K:c}\rangle$ to $|\mathrm{K:b}\rangle$ and, subsequently, to $|\mathrm{K:a}\rangle$.

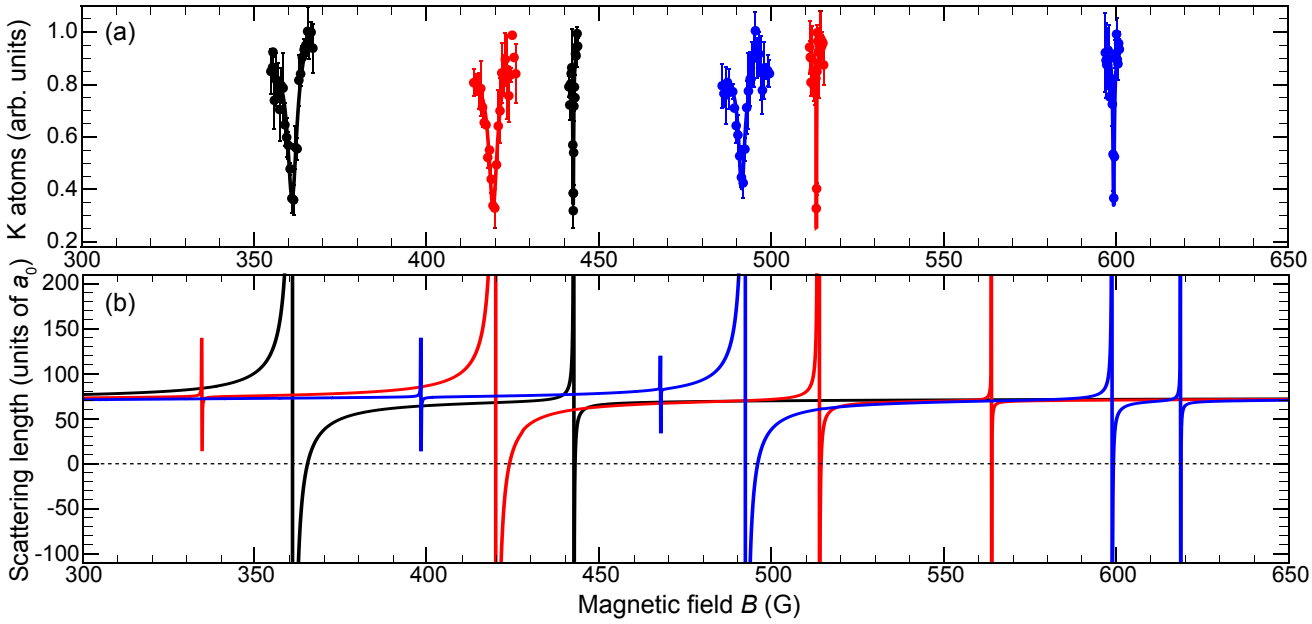

FIG. 3: Overview of ^{39}K-^{133}Cs interspecies Feshbach resonances. (a) Loss features for $|\mathrm{Cs:a}\rangle$ with $|\mathrm{K:a}\rangle$ (black), $|\mathrm{K:b}\rangle$ (red), and $|\mathrm{K:c}\rangle$ (blue). The data is normalized to the atom number away from resonance. (b) Calculated interspecies scattering length a for the three hyperfine state combinations as a function of magnetic field B, using the G2017 interaction potentials fitted in Section III C.

Each step takes place at $B = 35.5$ G within 25 ms with an efficiency close to unity. For each spin mixture we again detect a pair of resonances, one broader and the other narrower. All measured Feshbach resonances are shown in Fig. 3(a) and their parameters are summarized in Table I. We obtain the magnetic field B by measuring Cs microwave frequencies at the fields where interspecies loss features are observed. The experimental errors given in Table I are statistical errors from the Lorentzian fits. A drift of the magnetization of the stainless steel chamber, which depends on the offset field strength, gives rise to a systematic error on the order of ± 0.3 G.

III. THEORY

A. Computational methods for bound states and scattering

For the scattering and near-threshold bound states, we solve the Schrödinger equation by coupled-channel methods, using a basis set for the electron and nuclear spins in a fully decoupled representation,

$$|s_{\mathrm{K}} m_{s,\mathrm{K}}\rangle |i_{\mathrm{K}} m_{i,\mathrm{K}}\rangle |s_{\mathrm{Cs}} m_{s,\mathrm{Cs}}\rangle |i_{\mathrm{Cs}} m_{i,\mathrm{Cs}}\rangle |L M_L\rangle. \qquad (1)$$

The matrix elements of the different terms in the Hamiltonian in this basis set are given in the Appendix of Ref. [60]. The calculations in this paper used basis sets with all possible values of m_s and m_i for both atoms, subject to conservation of $M_{\mathrm{tot}} = m_{s,\mathrm{K}} + m_{i,\mathrm{K}} + m_{s,\mathrm{Cs}} + m_{i,\mathrm{Cs}} + M_L$. For s-wave scattering at a particular threshold, M_{tot} is set by the states of the incoming atoms, $M_{\mathrm{tot}} = m_{f,\mathrm{K}} + m_{f,\mathrm{Cs}}$.

Scattering calculations are carried out using the MOLSCAT package [61], as modified to handle collisions in magnetic fields [62]. At each magnetic field B, the wavefunction log-derivative matrix at collision energy E is propagated from $R = 5.6$ a_0 to 15 a_0 using the propagator of Manolopoulos [63] with a fixed step size of 0.001 a_0, and from 15 to 3,000 a_0 using the Airy propagator [64] with a variable step size controlled by the parameter TOLHI $= 10^{-5}$ [65]. Scattering boundary conditions [66] are applied at $R = 3,000$ a_0 to obtain the scattering S-matrix. The energy-dependent s-wave scattering length $a(k)$ is then obtained from the diagonal S-matrix element in the incoming $L = 0$ channel using the identity [67]

$$a(k) = \frac{1}{ik}\left(\frac{1 - S_{00}}{1 + S_{00}}\right), \qquad (2)$$

where $k^2 = 2\mu E/\hbar^2$ and μ is the reduced mass.

Weakly bound levels for Feshbach molecules are obtained using the propagation method described in Refs. [68] and [60], using the same step size as for MOLSCAT with a reduced propagation range of $R = 5.6$ a_0 to 1,000 a_0. Levels are located either as bound-state energies at a fixed value of the magnetic field B using the BOUND package [69] or as bound-state fields at a fixed value of the binding energy using the FIELD package [70]. BOUND and FIELD converge to values of the energy (or field) where the log-derivative matching matrix [68] has a zero eigenvalue. Both programs implement a node-count algorithm [68] which makes it straightforward to ensure that *all* bound states that exist in a particular range of energy or field are located.

Zero-energy Feshbach resonances can be located as fields $B_{\rm res}$ at which the scattering length $a(B)$ passes through a pole,

$$a(B) = a_{\rm bg}\left(1 - \frac{\Delta}{B - B_{\rm res}}\right). \quad (3)$$

MOLSCAT has the capability to converge on such poles to provide resonance widths Δ and background scattering lengths $a_{\rm bg}$ as well as resonance positions. However, when only resonance positions are required, the FIELD package provides a much cleaner approach: simply running FIELD at zero energy provides a complete list of the energies at which bound states cross threshold, and thus a complete list of resonance positions. The widths and background scattering lengths may then be obtained if required, using scattering calculations with MOLSCAT around the field concerned.

In the present work, basis sets including only $L = 0$ functions were used in most cases, since they make the calculations simpler at the b+a and c+a thresholds, where inelastic decay would otherwise exist. However, calculations with $L_{\rm max} = 2$ were used for the calculations of scattering and bound states on the fitted potentials in Section III D below. As will be seen, the observed resonances in the a+a channel shifted by no more than 0.01 G when $L = 2$ basis functions were included, which is considerably less than the experimental uncertainties in the resonance positions.

B. Potential curves

The KCs interaction potentials of Ferber *et al.* [53] (F2013) were fitted to extensive Fourier transform spectra of the KCs molecule, including vibrational levels up to $v = 102$ for the $X^1\Sigma^+$ singlet ground state and $v = 32$ for the $a^3\Sigma^+$ triplet state (although there is significant mixing of the singlet and triplet states for the highest vibrational levels). Each potential curve is constructed in three segments; the central segment from $R_S^{\rm SR}$ to $R_S^{\rm LR}$, with $S = 0$ or 1 for the singlet or triplet state, respectively, is represented as a power-series expansion in the variable $\xi(R) = (R - R_{\rm m})/(R + bR_{\rm m})$, where $R_{\rm m}$ is chosen to be near the equilibrium distance. At long range ($R > R_S^{\rm LR}$), the potentials are

$$V_S^{\rm LR}(R) = -C_6/R^6 - C_8/R^8 - C_{10}/R^{10} - (-1)^S V_{\rm exch}(R), \quad (4)$$

where the dispersion coefficients C_n [53, 71, 72] are common to both potentials. The exchange contribution is [73]

$$V_{\rm exch}(R) = A_{\rm ex} R^\gamma \exp(-\beta R), \quad (5)$$

and makes an attractive contribution for the singlet and a repulsive contribution for the triplet. The central segment is constrained to match the long-range potential at $R_S^{\rm LR}$. The potentials are extended to short range ($R < R_S^{\rm SR}$) with simple repulsive terms,

$$V_S^{\rm SR}(R) = A_S^{\rm SR} + B_S^{\rm SR}/R^{N_S^{\rm SR}}. \quad (6)$$

TABLE II: Quality of fit to the observed resonance positions, together with the properties of additional resonances predicted by the G2017 potentials. The uncertainties given here include systematic errors and are those that define the weights used in the least-squares fit.

threshold	$B_{\rm obs}$	$B_{\rm calc}$	$\Delta_{\rm calc}$	$B_{\rm obs} - B_{\rm calc}$	Unc.
a+a	361.1	360.74	4.4	0.36	0.4
a+a	442.59	442.43	0.37	0.16	0.3
b+a	419.3	419.73	4.0	−0.43	0.4
b+a	513.12	513.73	0.52	−0.61	0.3
c+a	491.5	492.24	3.6	−0.74	0.4
c+a	599.32	598.76	0.39	0.58	0.3
b+a		334.45	0.025		
b+a		563.81	0.074		
b+b		319.35	0.046		
c+a		398.09	0.023		
c+a		467.70	0.006		
c+a		618.71	0.094		

The parameters $A_S^{\rm SR}$ and $B_S^{\rm SR}$ are chosen to match the values and derivatives of the mid-range potentials at $R_S^{\rm SR}$. The potential matching points for KCs are $R_0^{\rm SR} = 3.22$ Å and $R_0^{\rm LR} = 12.00$ Å for the singlet state and $R_1^{\rm SR} = 5.23$ Å and $R_1^{\rm LR} = 12.01$ Å for the triplet state [53].

For coupled-channel calculations of the near-threshold bound states and scattering properties, these potentials are supplemented by a coupling $\hat{V}^{\rm d}(R)$, which at long range has a simple magnetic dipole-dipole form that varies as $1/R^3$ [74, 75]. However, for heavy atoms, second-order spin-orbit coupling provides an additional contribution that has the same tensor form as the dipole-dipole term. $\hat{V}^{\rm d}(R)$ is represented as

$$\hat{V}^{\rm d}(R) = \lambda(R)\left(\hat{s}_1 \cdot \hat{s}_2 - 3(\hat{s}_1 \cdot \vec{e}_R)(\hat{s}_2 \cdot \vec{e}_R)\right), \quad (7)$$

where $\vec{e}_R$ is a unit vector along the internuclear axis and λ is an R-dependent coupling constant,

$$\lambda(R) = E_{\rm h}\alpha^2\left[A_{\rm 2SO}^{\rm short}\exp\left(-\beta_{\rm 2SO}^{\rm short}(R/a_0)\right) + A_{\rm 2SO}^{\rm long}\exp\left(-\beta_{\rm 2SO}^{\rm long}(R/a_0)\right) + \frac{g_S^2}{4(R/a_0)^3}\right], \quad (8)$$

where $\alpha \approx 1/137$ is the atomic fine-structure constant, $E_{\rm h}$ is the Hartree energy and $g_S \approx 2.0023$ is the electron g-factor. The second-order spin-orbit coupling has not been obtained from electronic structure calculations for KCs, so in the present work we retained the estimate used in Ref. [54], obtained by shifting the RbCs function [76] inwards by $0.125\,a_0$, to give the same value at the inner turning point for KCs as for RbCs. This gives $\beta_{\rm 2SO}^{\rm short} = 0.80$ and $\beta_{\rm 2SO}^{\rm long} = 0.28$ as for RbCs, with $A_{\rm 2SO}^{\rm short} = -45.5$ and $A_{\rm 2SO}^{\rm long} = -0.032$.

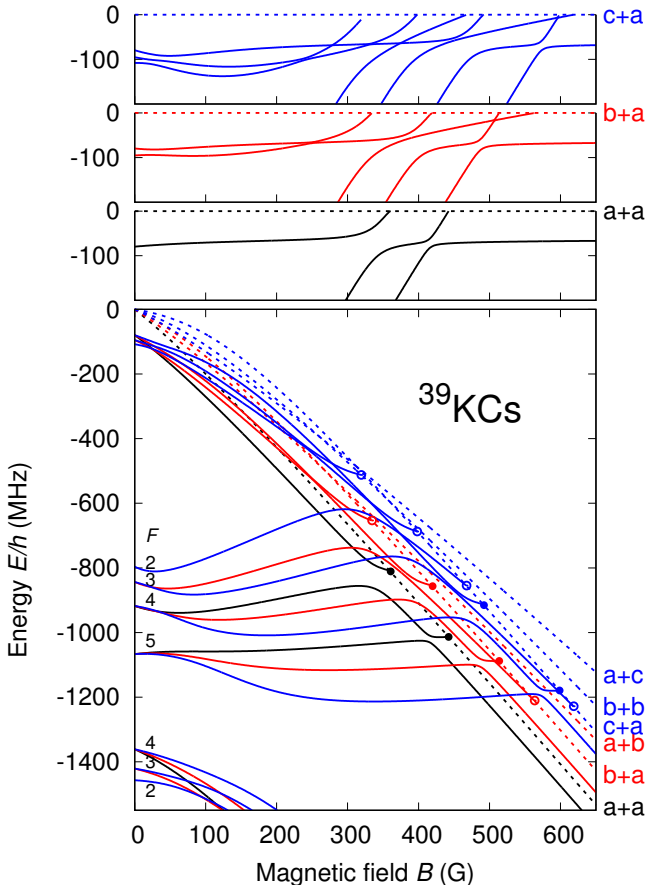

FIG. 4: Bottom panel: Bound states of ^{39}KCs (solid lines) with $M_F = 2$ (blue), 3 (red) and 4 (black), together with the corresponding thresholds (dashed lines), calculated using the G2017 fitted interaction potentials of Section III C with $L = 0$ functions only and shown with respect to the lowest zero-field threshold. The threshold crossings that produce observed resonances are shown with filled circles and those so far unobserved with open circles. Upper panels: Bound states for $M_F = 2$, 3 and 4, shown relative to the c+a, b+a and a+a thresholds.

C. Least-squares fitting

The resonances observed in the present work are due to s-wave bound states that cross threshold as a function of magnetic field. These are substantially broader than resonances due to d-wave and higher states [54]. Figure 4 shows the atomic thresholds for $M_F = m_{f,\mathrm{K}} + m_{f,\mathrm{Cs}} = 2$, 3 and 4, together with the s-wave bound states responsible for the resonances observed here, calculated on the G2017 fitted potentials described below. There is a state roughly parallel to each of the a+a, b+a and c+a thresholds, bound by 65 MHz to 70 MHz and with the same $(f_\mathrm{K}, m_{f,\mathrm{K}}, f_\mathrm{Cs}, m_{f,\mathrm{Cs}})$ character as the threshold. Crossing these near-threshold states are a set of deeper states, bound by 800 MHz to 1100 MHz at zero field, that are closer to horizontal in the bottom panel of Fig. 4. This second set of states correlates at zero field with atoms with $f_\mathrm{K} = 2$ and $f_\mathrm{Cs} = 3$, with resultant $F = 1$, 2, 3, 4, 5 (though $F = 1$ does not appear in Fig. 4 because states with $M_F < 2$ are not shown). The observed resonances occur when the near-threshold states are pushed across threshold by mixing with the near-horizontal states at broad avoided crossings, which are complete to varying extents at threshold. The positions of the resonances are thus principally determined by the binding energies of the near-horizontal states, although the states actually crossing threshold have mixed character. An analogous figure showing the bound states on the F2013 potentials [53] is included in the Supplemental Material [77]; the pattern of states is visually very similar, despite that fact that the sign of $a_\mathrm{s} - a_\mathrm{t}$ is reversed on the older potential.

The right-hand columns of Table I give the calculated positions and widths of the observed resonances, obtained using the F2013 potentials. It may be seen that the calculated resonance positions are all about 20 G lower than experiment. It is therefore desirable to adjust the interaction potentials to reproduce the resonance positions. In doing this, we wish to retain as much as possible of the spectroscopically determined potentials of Ref. [53], so that the fit to the Fourier transform spectra is affected as little as possible. We found in initial fitting that it is possible to reproduce the scattering properties by retaining the central and long-range parts of the spectroscopic potential curves and adjusting only the short-range parts for $R < R_S^\mathrm{SR}$. Small changes to the potential curves in this region have relatively little effect on levels with inner turning points below $V_0(R_0^\mathrm{SR})/hc = -316.6$ cm^{-1} for the singlet state and $V_1(R_1^\mathrm{SR})/hc = -116.1$ cm^{-1} for the triplet state. We explored modifications to the values of N_S^SR, with corresponding changes in A_S^SR and B_S^SR to match the values and derivatives of the power-series expansions at $R = R_S^\mathrm{SR}$,

$$\begin{aligned} B_S^\mathrm{SR} &= -\left(\frac{(R_S^\mathrm{SR})^{N_S^\mathrm{SR}+1}}{N_S^\mathrm{SR}}\right)\left(\frac{dV_S}{dR}\right)_{R=R_S^\mathrm{SR}}; \\ A_S^\mathrm{SR} &= V_S(R_S^\mathrm{SR}) - B_S^\mathrm{SR}/(R_S^\mathrm{SR})^{N_S^\mathrm{SR}}. \end{aligned} \qquad (9)$$

We have carried out least-squares fits of potential parameters to the observed resonance positions using the I-NoLLS package [78] (Interactive Non-Linear Least-Squares), which gives the user interactive control over step lengths and assignments as the fit proceeds. The quantity optimized in the least-squares fits was the sum of squares of residuals ((observed − calculated)/uncertainty), with the uncertainties listed in Table II. The resonance positions at the a+a, b+a and c+a thresholds are principally sensitive to the triplet potential, so our initial fits varied N_1^SR only, leaving the singlet potential unchanged. The optimum fit was obtained with $N_1^\mathrm{SR} = 6.9(1)$ and gives the fit to the resonance positions shown in Table II. The short-range coefficients for the best-fit triplet potential are obtained from Eq. 9; their approximate values are $A_1^\mathrm{SR}/hc \approx -471.5728$ cm^{-1} and $B_1^\mathrm{SR}/hc \approx 3.224735 \times 10^7$ cm^{-1} Å$^{N_1^\mathrm{SR}}$.

We subsequently explored 2-parameter fits, varying both N_0^SR and N_1^SR. However, these produced no significant improvement in the quality of fit. A single-parameter fit varying only N_0^SR was incapable of reproducing the observed resonance positions. We therefore decided to proceed with the

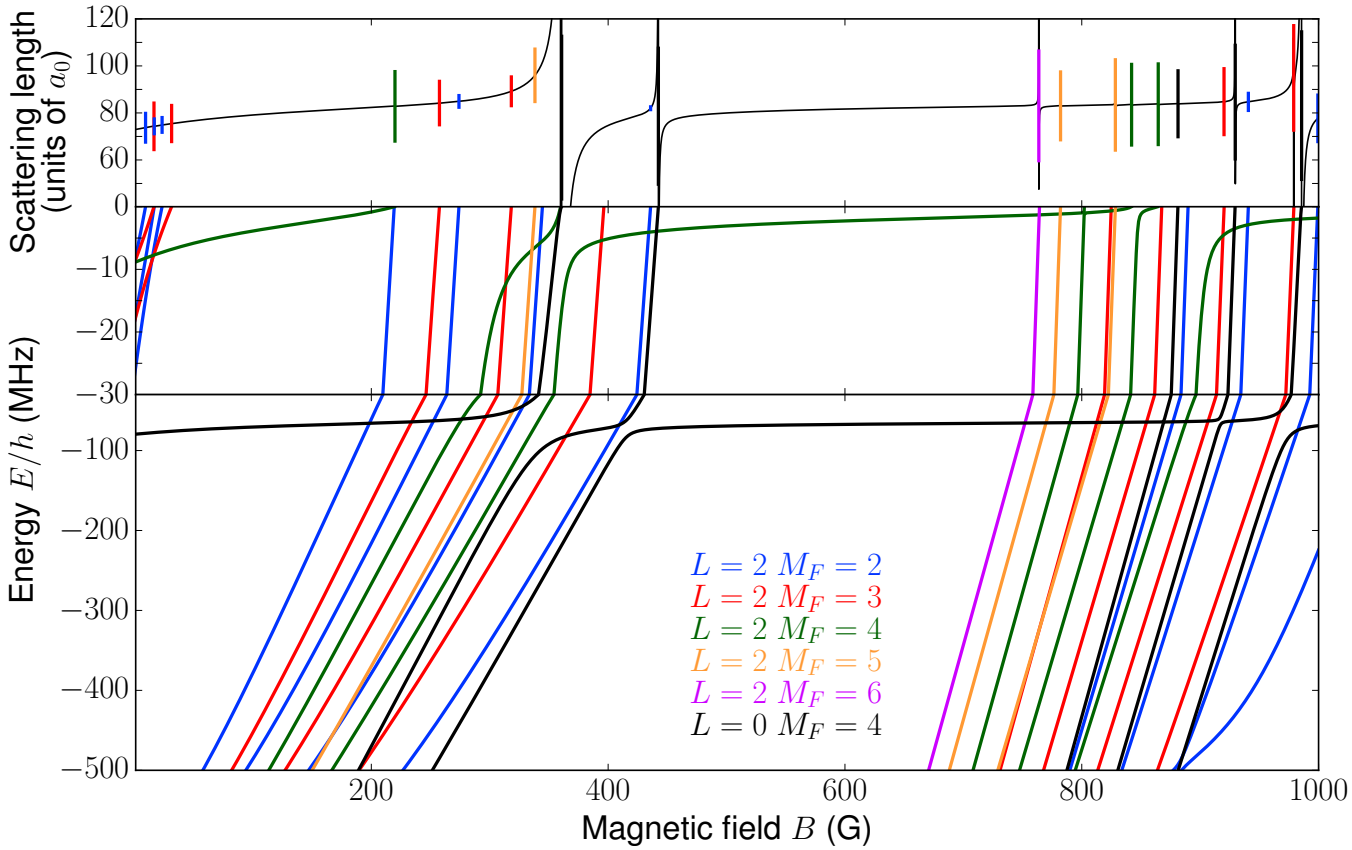

FIG. 5: Scattering length in the a+a channel and energies of near-threshold bound states for ^{39}KCs. Note that the top 30 MHz is shown on an expanded scale. Resonance widths greater than 1 μG are shown as vertical bars with lengths proportional to $\log(\Delta/\mu\mathrm{G})$.

TABLE III: Calculated singlet and triplet scattering lengths for isotopologs of KCs, with 1-σ statistical uncertainties for a_t.

	a_s (a_0)	a_t (a_0) G2017 potentials	a_t (a_0) F2013 potentials
^{39}KCs	−18.37	74.88(9)	82.24
^{40}KCs	−51.44	−71.67(45)	−41.28
^{41}KCs	−72.79	179.06(28)	205.25

single-parameter fit obtained by varying only the triplet potential, which we designate the G2017 potentials; a more extensive refinement will require additional experimental results.

It may be noted that the present modification shifts the vibrational levels of the $a^3\Sigma^+$ state by a maximum of about 0.1 cm^{-1}; this shift is less than 0.01 cm^{-1} below $v = 11$ and peaks around $v = 22$. These shifts are smaller than the Cs hyperfine splitting, but larger than the typical experimental uncertainties of 0.01 cm^{-1} in Ref. [53]. A more complete treatment would require refitting the entire potentials, but is not justified at this stage.

D. Calculations on optimized potentials

Figures 5 to 7 show the scattering lengths and resonance positions, calculated at the lowest (a+a) threshold for all three isotopic combinations of KCs using the optimized G2017 potentials, together with the near-threshold bound states that produce the resonances. Table III gives the predicted singlet and triplet scattering lengths a_s and a_t, together with the statistical uncertainty of a_t in the 1-parameter space. However, a_t may change outside these limits when additional parameters are fitted. Complete lists of the resonance parameters (positions, widths and background scattering lengths) are given in the Supplemental Material [77].

The G2017 potentials obtained here predict scattering and bound-state properties that differ in some important ways from those of Ref. [54]. In particular, the triplet scattering lengths all shift to smaller (or more negative) values, and the corresponding near-threshold levels are more deeply bound.

Figure 4 shows that, in addition to the two resonances currently observed in each of the a+a, b+a and c+a channels, there are additional ^{39}KCs resonances due to s-wave states in the b+a, c+a and b+b channels (where b+b is the lowest $M_F = 2$ threshold at fields between 261 G and 358 G). The positions and widths of these are included in Table II. They have predicted widths between 6 mG and 0.1 G, and may be useful for

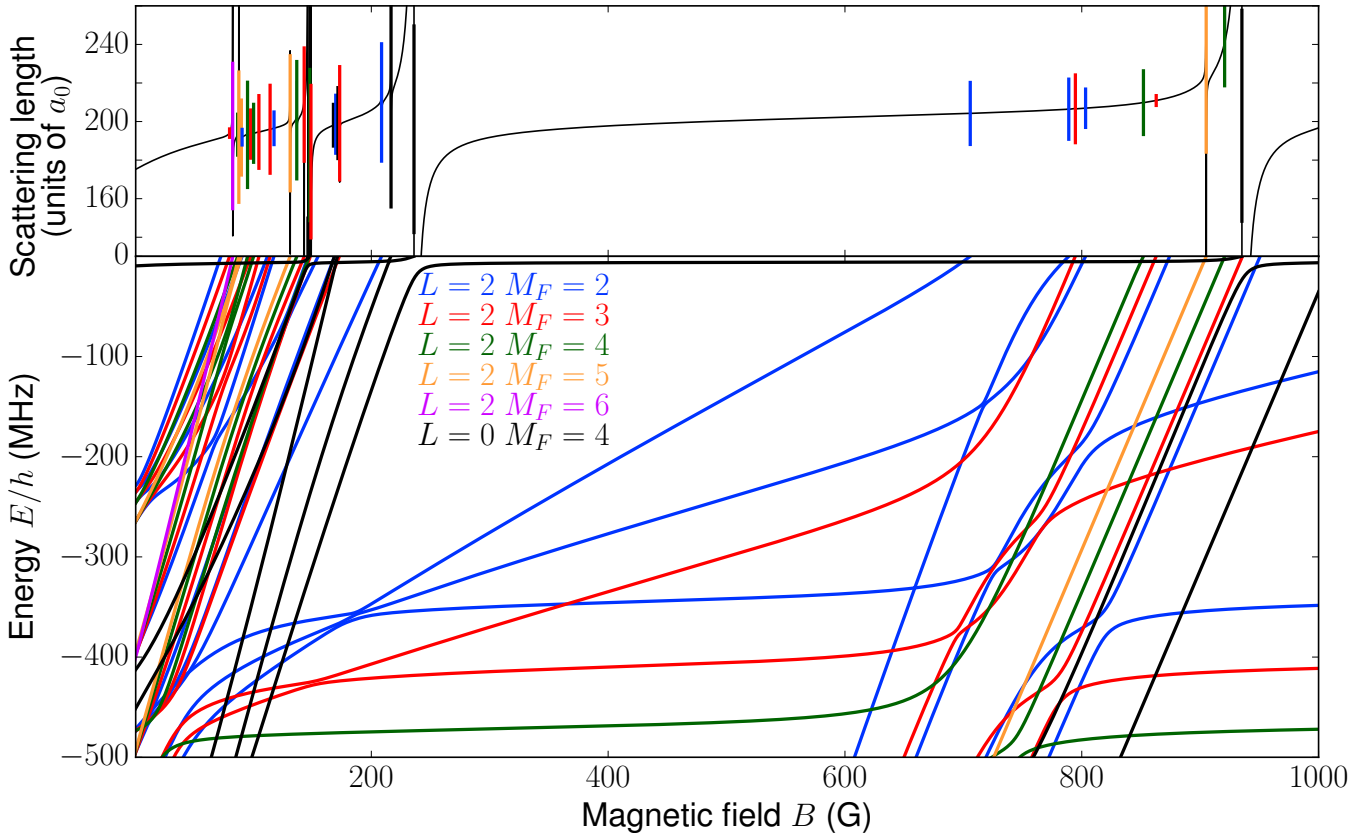

FIG. 6: Scattering length in the a+a channel and energies of near-threshold bound states for ^{41}KCs. Resonance widths greater than 1 μG are shown as vertical bars with lengths proportional to $\log(\Delta/\mu\mathrm{G})$.

molecule formation.

For ^{39}KCs, Ref. [54] predicted a group of low-field resonances at fields below 50 G, due to a group of d-wave states bound by less than 20 MHz at zero field. The widest of these was a resonance predicted near 50 G with a width of 1 mG, due to a state that was bound by less than 3 MHz at zero field but was nearly parallel to threshold as a function of field. On the G2017 potentials the corresponding states are significantly deeper; the state responsible for the widest resonance is now bound by about 9 MHz at zero field, and the resulting resonance is shifted to 219 G, now with a width of 0.7 mG. Similarly, for ^{41}KCs, Ref. [54] predicted a group of low-field resonances at fields of 20 G to 30 G, again due to a group of very weakly bound d-wave states. These looked promising for molecule formation because of their proximity to the region around 21 G where Cs can be cooled to degeneracy. On the G2017 potentials, however, these states are again significantly deeper, and the resonances are shifted to fields above 70 G.

For fermionic ^{40}KCs, by contrast, the G2017 potentials appear to offer improved prospects for molecule formation. The older F2013 potentials [53] give scattering lengths $a_\mathrm{s} = -51.44\ a_0$ and $a_\mathrm{t} = -41.28\ a_0$. Because these are so similar, even resonances due to s-wave states were predicted in Ref. [54] to be very narrow and those due to d-wave states even narrower. The G2017 potential, however, has $a_\mathrm{t} = -71.67\ a_0$. Because of this, the resonances are shifted to rather higher fields, but they are also considerably broader. For example, the resonance predicted in Ref. [54] at 264.3 G with a width of -0.1 G occurs at 286.0 G on the G2017 potentials with a width of -0.86 G. Similarly, the resonance previously predicted at 470 G with a width of -10 mG is now at 531 G, with a width of -54 mG. The latter is particularly promising for molecule formation, because it is reasonably close to the region around 556 G where Cs has a moderate scattering length [79] and can be cooled efficiently.

IV. CONCLUSION

We have observed Feshbach resonances due to s-wave bound states in ultracold collisions of ^{39}K and Cs. The resonances occur at magnetic fields about 20 G higher than those predicted in Refs. [53] and [54] using interaction potentials fitted to high-resolution Fourier transform spectra. Reproducing the experimental resonance positions requires a significant change to the triplet interaction potential of Ref. [53]. We have carried out least-squares fits to determine a triplet potential with a modified repulsive wall, which reproduces the Feshbach resonance positions while making only small changes to the deeper vibrational levels.

We have used the modified interaction potentials, which we

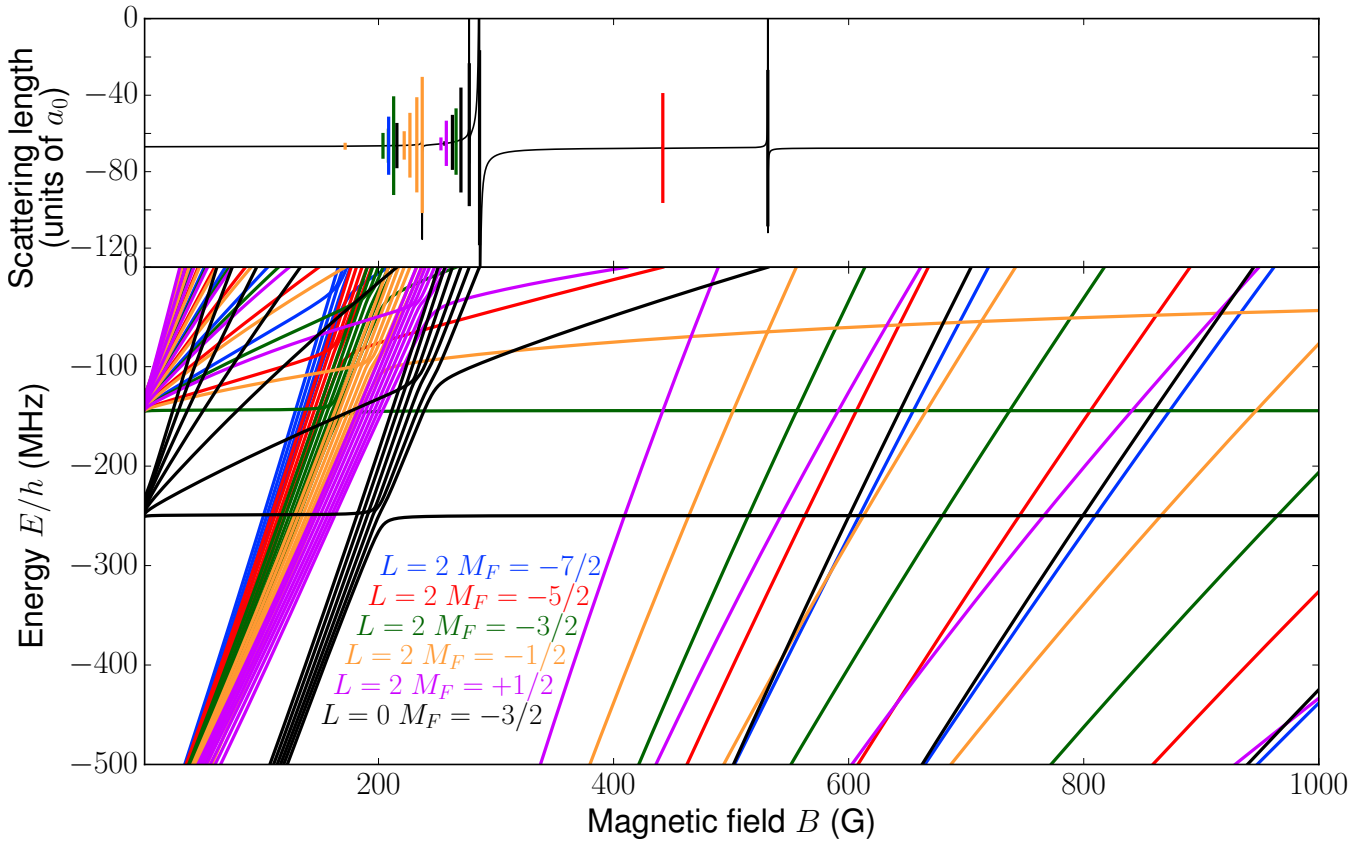

FIG. 7: Scattering length in the a+a channel and energies of near-threshold bound states for ^{40}KCs. Resonance widths greater than 1 μG are shown as vertical bars with lengths proportional to $\log(\Delta/\mu\mathrm{G})$.

designate G2017, to carry out coupled-channels calculations and make improved predictions of the near-threshold bound states and ultracold scattering properties for all three isotopes of K interacting with Cs. For the case of ^{40}KCs, the scattering properties are more favorable using the G2017 potentials than was found in Refs. [53] and [54]. In particular, the G2017 potentials predict a Feshbach resonance that is broad enough to allow tuning of the interactions in a K-Cs Fermi-Bose mixture. The results open up various interesting avenues in cold atom and cold molecule research. These include studies of the dynamics and transport properties of bosonic impurities in low-dimensional Fermi gases, similar to recent experiments where Bloch-type oscillations have been observed for impurity motion in a fermionized 1D Bose gas [18]. It may also be possible to form fermionic KCs molecules and transfer them to the rovibrational ground state to generate dipolar quantum gases, employing techniques such as those recently demonstrated for fermionic KRb [43] and for bosonic RbCs [39].

V. ACKNOWLEDGMENTS

We are indebted to R. Grimm for generous support. We thank G. Anich, K. Jag-Lauber, F. Meinert, and G. Unnikrishnan for fruitful discussions. We gratefully acknowledge funding by the European Research Council (ERC) under Project No. 278417, by the Austrian Science Foundation (FWF) under Project No. I1789-N20 (joint Austrian-French FWF-ANR project) and under Project No. P29602-N36 and by the UK Engineering and Physical Sciences Research Council under Grant No. EP/N007085/1.

[1] C. Chin, R. Grimm, P. S. Julienne, and E. Tiesinga, Rev. Mod. Phys. **82**, 1225 (2010).
[2] S. L. Cornish, N. R. Claussen, J. L. Roberts, E. A. Cornell, and C. E. Wieman, Phys. Rev. Lett. **85**, 1795 (2000).
[3] E. A. Donley, N. R. Clausen, S. L. Cornish, J. L. Roberts, E. A. Cornell, and C. E. Wieman, Nature **412**, 295 (2001).
[4] T. Weber, J. Herbig, M. Mark, H.-C. Nägerl, and R. Grimm, Science **299**, 232 (2003).
[5] E. A. Donley, N. R. Claussen, S. T. Thompson, and C. E. Wieman, Nature **417**, 529 (2002).
[6] C. A. Regal, C. Ticknor, J. L. Bohn, and D. S. Jin, Nature **424**, 47 (2003).
[7] J. Herbig, T. Kraemer, M. Mark, T. Weber, C. Chin, H.-C. Nägerl, and R. Grimm, Science **301**, 1510 (2003).

[8] S. Jochim, M. Bartenstein, A. Altmeyer, G. Hendl, S. Riedl, C. Chin, J. Hecker Denschlag, and R. Grimm, Science **302**, 2101 (2003).

[9] M. Greiner, C. A. Regal, and D. S. Jin, Nature **426**, 537 (2003).

[10] C. A. Regal, M. Greiner, and D. S. Jin, Phys. Rev. Lett. **92**, 040403 (2004).

[11] M. Bartenstein, A. Altmeyer, S. Riedl, S. Jochim, C. Chin, J. H. Denschlag, and R. Grimm, Phys. Rev. Lett. **92**, 120401 (2004).

[12] M. W. Zwierlein, C. A. Stan, C. H. Schunck, S. M. F. Raupach, A. J. Kerman, and W. Ketterle, Phys. Rev. Lett. **92**, 120403 (2004).

[13] T. Kraemer, M. Mark, P. Waldburger, J. G. Danzl, C. Chin, B. Engeser, A. D. Lange, K. Pilch, A. Jaakkola, H.-C. Nägerl, et al., Nature **440**, 315 (2006).

[14] A. Schirotzek, C.-H. Wu, A. Sommer, and M. W. Zwierlein, Phys. Rev. Lett. **102**, 230402 (2009).

[15] M. Koschorreck, D. Pertot, E. Vogt, B. Fröhlich, M. Feld, and M. Köhl, Nature **485**, 619 (2012).

[16] E. Haller, M. Gustavsson, M. J. Mark, J. G. Danzl, R. Hart, G. Pupillo, and H. C. Nägerl, Science **325**, 1224 (2009).

[17] E. Haller, R. Hart, M. J. Mark, J. G. Danzl, L. Reichsöllner, M. Gustavsson, M. Dalmonte, G. Pupillo, and H.-C. Nägerl, Nature **466**, 597 (2010).

[18] F. Meinert, M. Knap, E. Kirilov, K. Jag-Lauber, M. B. Zvonarev, E. Demler, and H.-C. Nägerl, arXiv:1608.08200 (2016).

[19] I. Titvinidze, M. Snoek, and W. Hofstetter, Phys. Rev. Lett. **100**, 100401 (2008).

[20] L. J. Wacker, N. B. Jørgensen, D. Birkmose, N. Winter, M. Mikkelsen, J. Sherson, N. Zinner, and J. J. Arlt, Phys. Rev. Lett. **117**, 163201 (2016).

[21] J. Ulmanis, S. Häfner, R. Pires, E. D. Kuhnle, Y. Wang, C. H. Greene, and M. Weidemüller, Phys. Rev. Lett. **117**, 153201 (2016).

[22] G. Barontini, C. Weber, F. Rabatti, J. Catani, G. Thalhammer, M. Inguscio, and F. Minardi, Phys. Rev. Lett. **103**, 043201 (2009).

[23] D. V. Efremov and L. Viverit, Phys. Rev. B **65**, 134519 (2002).

[24] M. Lewenstein, L. Santos, M. A. Baranov, and H. Fehrmann, Phys. Rev. Lett. **92**, 050401 (2004).

[25] I. Ferrier-Barbut, M. Delehaye, S. Laurent, A. T. Grier, M. Pierce, B. S. Rem, F. Chevy, and C. Salomon, Science **345**, 1035 (2014).

[26] K.-K. Ni, S. Ospelkaus, M. H. G. de Miranda, A. Pe'er, B. Neyenhuis, J. J. Zirbel, S. Kotochigova, P. S. Julienne, D. S. Jin, and J. Ye, Science **322**, 231 (2008).

[27] M. Baranov, M. Dalmonte, G. Pupillo, and P. Zoller, Chem. Rev. **112**, 5012 (2012).

[28] T. Lahaye, C. Menotti, L. Santos, M. Lewenstein, and T. Pfau, Rep. Prog. Phys. **72**, 126401 (2009).

[29] B. Capogrosso-Sansone, C. Trefzger, M. Lewenstein, P. Zoller, and G. Pupillo, Phys. Rev. Lett. **104**, 125301 (2010).

[30] A. Micheli, G. Pupillo, H. P. Büchler, and P. Zoller, Phys. Rev. A **76**, 043604 (2007).

[31] C. Trefzger, C. Menotti, B. Capogrosso-Sansone, and M. Lewenstein, J. Phys. B **44**, 193001 (2011).

[32] C. Trefzger, C. Menotti, and M. Lewenstein, Phys. Rev. Lett. **103**, 035304 (2009).

[33] K. Bergmann, H. Theuer, and B. W. Shore, Rev. Mod. Phys. **70**, 1003 (1998).

[34] J. G. Danzl, E. Haller, M. Gustavsson, M. J. Mark, R. Hart, N. Bouloufa, O. Dulieu, H. Ritsch, and H.-C. Nägerl, Science **321**, 1062 (2008).

[35] K.-K. Ni, S. Ospelkaus, M. H. G. de Miranda, A. Pe'er, B. Neyenhuis, J. J. Zirbel, S. Kotochigova, P. S. Julienne, D. S. Jin, and J. Ye, Science **322**, 231 (2008).

[36] J. W. Park, S. A. Will, and M. W. Zwierlein, Phys. Rev. Lett. **114**, 205302 (2015).

[37] T. Takekoshi, L. Reichsöllner, A. Schindewolf, J. M. Hutson, C. R. Le Sueur, O. Dulieu, F. Ferlaino, R. Grimm, and H.-C. Nägerl, Phys. Rev. Lett. **113**, 205301 (2014).

[38] P. K. Molony, P. D. Gregory, Z. Ji, B. Lu, M. P. Köppinger, C. R. Le Sueur, C. L. Blackley, J. M. Hutson, and S. L. Cornish, Phys. Rev. Lett. **113**, 255301 (2014).

[39] L. Reichsöllner, A. Schindewolf, T. Takekoshi, R. Grimm, and H.-C. Nägerl, arXiv:1607.06536 (2016).

[40] M. Guo, B. Zhu, B. Lu, X. Ye, F. Wang, R. Vexiau, N. Bouloufa-Maafa, G. Quéméner, O. Dulieu, and D. Wang, Phys. Rev. Lett. **116**, 205303 (2016).

[41] M. Aymar and O. Dulieu, J. Chem. Phys. **122**, 204302 (2005).

[42] P. S. Żuchowski and J. M. Hutson, Phys. Rev. A **81**, 060703 (2010).

[43] S. A. Moses, J. P. Covey, M. T. Miecnikowski, B. Yan, B. Gadway, J. Ye, and D. S. Jin, Science **350**, 659 (2015).

[44] C. D'Errico, M. Zaccanti, M. Fattori, G. Roati, M. Inguscio, G. Modugno, and A. Simoni, New J. Phys. **9**, 223 (2007).

[45] P. J. Leo, C. J. Williams, and P. S. Julienne, Phys. Rev. Lett. **85**, 2721 (2000).

[46] M. Berninger, A. Zenesini, B. Huang, W. Harm, H.-C. Nägerl, F. Ferlaino, R. Grimm, P. S. Julienne, and J. M. Hutson, Phys. Rev. A **87**, 032517 (2013).

[47] T. Weber, J. Herbig, M. Mark, H.-C. Nägerl, and R. Grimm, Science **299**, 232 (2003).

[48] G. Roati, M. Zaccanti, C. D'Errico, J. Catani, M. Modugno, A. Simoni, M. Inguscio, and G. Modugno, Phys. Rev. Lett. **99**, 010403 (2007).

[49] M. Landini, S. Roy, G. Roati, A. Simoni, M. Inguscio, G. Modugno, and M. Fattori, Phys. Rev. A **86**, 033421 (2012).

[50] G. Salomon, L. Fouché, S. Lepoutre, A. Aspect, and T. Bourdel, Phys. Rev. A **90**, 033405 (2014).

[51] M. Gröbner, P. Weinmann, F. Meinert, K. Lauber, E. Kirilov, and H.-C. Nägerl, J. Mod. Optic. **63**, 1829 (2016).

[52] R. Ferber, I. Klincare, O. Nikolayeva, M. Tamanis, H. Knöckel, E. Tiemann, and A. Pashov, Phys. Rev. A **80**, 062501 (2009).

[53] R. Ferber, O. Nikolayeva, M. Tamanis, H. Knöckel, and E. Tiemann, Phys. Rev. A **88**, 012516 (2013).

[54] H. J. Patel, C. L. Blackley, S. L. Cornish, and J. M. Hutson, Phys. Rev. A **90**, 032716 (2014).

[55] T. Weber, J. Herbig, M. Mark, H.-C. Nägerl, and R. Grimm, Science **299**, 232 (2003).

[56] G. Roati, M. Zaccanti, C. D'Errico, J. Catani, M. Modugno, A. Simoni, M. Inguscio, and G. Modugno, Phys. Rev. Lett. **99**, 010403 (2007).

[57] M. Landini, S. Roy, L. Carcagní, D. Trypogeorgos, M. Fattori, M. Inguscio, and G. Modugno, Phys. Rev. A **84**, 043432 (2011).

[58] P. Treutlein, K. Y. Chung, and S. Chu, Phys. Rev. A **63**, 051401 (2001).

[59] T. Kraemer, J. Herbig, M. Mark, T. Weber, C. Chin, H.-C. Nägerl, and R. Grimm, Appl. Phys. B **79**, 1013 (2004).

[60] J. M. Hutson, E. Tiesinga, and P. S. Julienne, Phys. Rev. A **78**, 052703 (2008), note that the matrix element of the dipolar spin-spin operator given in Eq. A2 of this paper omits a factor of $-\sqrt{30}$.

[61] J. M. Hutson and S. Green, *MOLSCAT computer program, version 14*, distributed by Collaborative Computational Project No. 6 of the UK Engineering and Physical Sciences Research Council (1994).

[62] M. L. González-Martínez and J. M. Hutson, Phys. Rev. A **75**,

022702 (2007).
[63] D. E. Manolopoulos, J. Chem. Phys. **85**, 6425 (1986).
[64] M. H. Alexander and D. E. Manolopoulos, J. Chem. Phys. **86**, 2044 (1987).
[65] M. H. Alexander, J. Chem. Phys. **81**, 4510 (1984).
[66] B. R. Johnson, J. Comput. Phys. **13**, 445 (1973).
[67] J. M. Hutson, New J. Phys. **9**, 152 (2007).
[68] J. M. Hutson, Comput. Phys. Commun. **84**, 1 (1994).
[69] J. M. Hutson, *BOUND computer program, version 5*, distributed by Collaborative Computational Project No. 6 of the UK Engineering and Physical Sciences Research Council (1993).
[70] J. M. Hutson, *FIELD computer program, version 1* (2011).
[71] A. Derevianko, J. F. Babb, and A. Dalgarno, Phys. Rev. A **63**, 052704 (2001).
[72] S. G. Porsev and A. Derevianko, J. Chem. Phys. **119**, 844 (2003).
[73] B. M. Smirnov and M. I. Chibisov, Sov. Phys. JETP **21**, 624 (1965).
[74] H. T. C. Stoof, J. M. V. A. Koelman, and B. J. Verhaar, Phys. Rev. B **38**, 4688 (1988).
[75] A. J. Moerdijk, B. J. Verhaar, and A. Axelsson, Phys. Rev. A **51**, 4852 (1995).
[76] T. Takekoshi, M. Debatin, R. Rameshan, F. Ferlaino, R. Grimm, H.-C. Nägerl, C. R. Le Sueur, J. M. Hutson, P. S. Julienne, S. Kotochigova, et al., Phys. Rev. A **85**, 032506 (2012).
[77] See Supplemental Material at [to be inserted by publisher].
[78] M. M. Law and J. M. Hutson, Comput. Phys. Commun. **102**, 252 (1997).
[79] M. Berninger, A. Zenesini, B. Huang, W. Harm, H.-C. Nägerl, F. Ferlaino, R. Grimm, P. S. Julienne, and J. M. Hutson, Phys. Rev. A **87**, 032517 (2013).

VI. SUPPLEMENTAL MATERIAL: OBSERVATION OF INTERSPECIES FESHBACH RESONANCES IN AN ULTRACOLD ^{39}K-^{133}CS MIXTURE AND REFINEMENT OF INTERACTION POTENTIALS

TABLE IV: Supplementary Table I. Resonance properties predicted from the optimized G2017 potentials for the a+a channel of ^{39}KCs, with the positions from Ref. [54] for comparison. Resonances were located using MOLSCAT, with R_{max} set to 1,500 a_0.

B_0 (G) G2017 potentials	B_0 (G) F2013 potentials	Δ (G) G2017 potentials	a_{bg} (a_0) G2017 potentials	L	M_F
9.335	2.995	1.5×10^{-5}	63.7	2	2
16.450	5.482	8×10^{-5}	64.3	2	3
16.670	10.784	4×10^{-6}	64.3	2	2
23.293	16.311	4×10^{-6}	64.9	2	2
31.344	18.154	3×10^{-5}	65.5	2	3
219.346	202.900	6×10^{-7}	72.9	2	2
219.972	49.593	7×10^{-4}	72.8	2	4
257.539	240.221	6×10^{-5}	74.2	2	3
274.019	255.726	3×10^{-6}	74.9	2	2
318.249	298.576	1.5×10^{-5}	79.2	2	3
338.197	318.143	1.4×10^{-4}	86.0	2	5
344.508	323.897	6×10^{-7}	91.5	2	2
359.899	326.943	0.012	420	2	4
360.745	341.895	4.6	68	0	4
396.419	373.849	3×10^{-7}	63.8	2	3
435.855	412.433	1.3×10^{-6}	72.0	2	2
442.429	421.364	0.37	68.6	0	4
763.737	697.020	0.031	73.0	2	6
782.083	714.609	6×10^{-4}	73.0	2	5
802.159	375.354	5×10^{-7}	73.2	2	4
824.886	757.456	4×10^{-10}	73.5	2	3
828.375	760.131	0.005	73.4	2	5
842.083	734.709	0.002	73.5	2	4
864.584	778.978	0.002	73.7	2	4
867.490	798.340	7×10^{-8}	73.7	2	3
881.298	813.139	5×10^{-4}	73.9	0	4
889.799	819.977	7×10^{-8}	74.0	2	2
920.147	849.801	5×10^{-4}	74.8	2	3
929.603	860.524	0.045	74.6	0	4
940.700	869.412	5×10^{-6}	74.7	2	2
978.997	907.538	0.019	84.9	2	3
985.676	915.564	1.1	73.1	0	4
999.386	926.772	8×10^{-5}	67.7	2	2

TABLE V: Supplementary Table II. Resonance properties predicted from the optimized G2017 potentials for the a+a channel of ^{41}KCs, with the positions from Ref. [54] for comparison. Resonances were located using MOLSCAT, with $R_{\max}$ set to 1,500 a_0.

B_0 (G) G2017 potentials	B_0 (G) F2013 potentials	Δ (G) G2017 potentials	$a_{\rm bg}$ (a_0) G2017 potentials	L	M_F
72.950	50.848	6×10^{-7}	171.5	2	2
80.281	47.266	1.8×10^{-6}	174.0	2	3
82.902	23.890	0.029	172.5	2	6
87.111	53.035	1.8×10^{-5}	173.2	2	4
88.120	25.677	0.010	171.9	2	5
90.238	39.244	2×10^{-4}	171.7	2	5
90.866	56.608	3×10^{-6}	171.9	2	2
95.460	42.860	1.7×10^{-3}	173.1	2	4
98.090	55.545	3×10^{-5}	173.5	2	3
100.577	28.413	6×10^{-5}	173.9	2	4
105.056	32.104	1.7×10^{-4}	174.6	2	3
112.269	68.538	2×10^{-8}	175.6	2	2
114.513	64.875	5×10^{-4}	176.0	2	3
117.826	36.635	1.0×10^{-5}	176.5	2	2
131.464	90.098	0.014	179.1	2	5
137.038	98.542	0.004	180.7	2	4
143.299	108.839	0.003	188.8	2	3
146.325	98.503	0.051	345	2	2
146.492	113.926	0.15	86.2	0	4
148.031	87.381	0.044	167.8	2	4
149.012	94.276	0.048	159.2	2	3
155.171	126.591	9×10^{-7}	173.0	2	2
168.004	120.590	1.9×10^{-5}	178.1	0	4
169.953	91.559	6×10^{-5}	178.6	2	2
171.823	111.038	1.5×10^{-4}	179.2	0	4
173.280	90.442	0.003	179.1	2	3
208.658	109.860	0.004	189.9	2	2
216.655	171.198	0013	195.8	0	4
236.047	168.192	2.2	176	0	4
705.820	629.690	8×10^{-5}	184.2	2	2
789.035	737.859	7×10^{-5}	186.4	2	2
794.615	746.956	1.2×10^{-4}	186.6	2	3
803.232	755.110	1.5×10^{-5}	186.9	2	2
852.093	806.405	9×10^{-5}	189.8	2	4
862.873	818.335	2×10^{-6}	190.9	2	3
874.210	830.925	4.4×10^{-9}	192.4	2	2
905.078	861.029	2.8×10^{-2}	201.7	2	5
920.652	877.705	4.3×10^{-4}	220.8	2	4
935.245	884.925	3.0	183	0	4
935.745	894.133	-1.8×10^{-5}	-909	2	3
950.626	910.602	1.6×10^{-10}	148.3	2	2

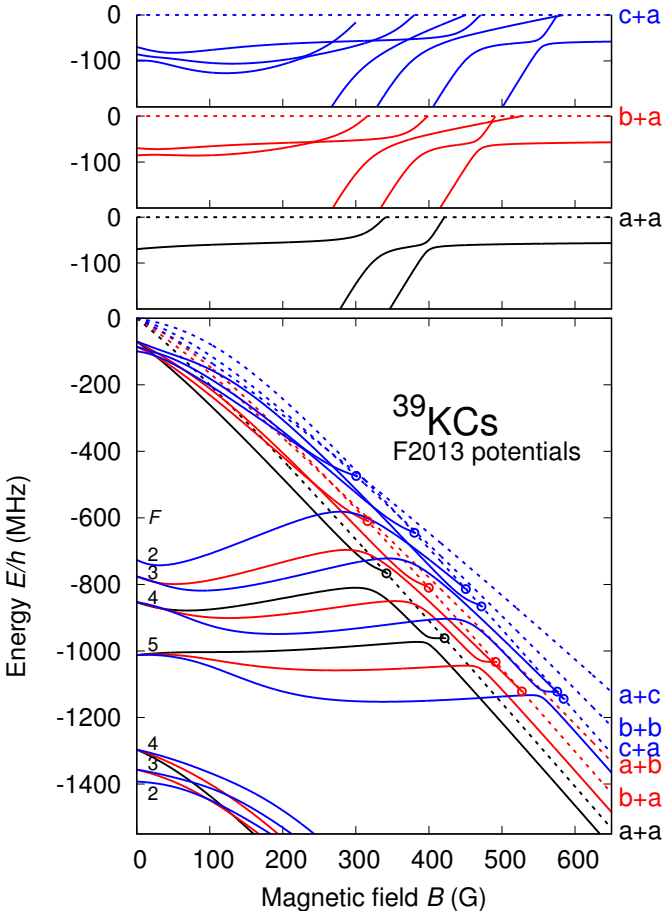

FIG. 8: Supplementary Figure 1. Bottom panel: Bound states of ^{39}KCs (solid lines) with $M_F = 2$ (blue), 3 (red) and 4 (black), together with the corresponding thresholds (dashed lines), calculated using the interaction potentials of Ref. [53] with $L = 0$ functions only and shown with respect to the lowest zero-field threshold. Upper panels: Bound states for $M_F = 2$, 3 and 4, shown relative to the c+a, b+a and a+a thresholds.

TABLE VI: Supplementary Table III. Resonance properties predicted from the optimized potentials for the a+a channel of ^{40}KCs, with the positions from Ref. [54] for comparison. Resonances with widths tabulated were located using MOLSCAT, with $R_{\rm max}$ set to 1,500 a_0; those without tabulated widths proved impossible to locate using MOLSCAT and must be much narrower than 1 nG. Their tabulated positions are those of the threshold crossings identified by FIELD. Because of mixing between bound states, the mapping between resonances on the G2017 and F2013 potentials is uncertain for some resonances below 200 G.

B_0 (G) G2017 potentials	B_0 (G) F2013 potentials	Δ (G) G2017 potentials	$a_{\rm bg}$ (a_0) G2017 potentials	L	M_F
31.002	27.103		−66.9	2	+1/2
32.923	29.035	-1.0×10^{-13}	−66.9	2	-1/2
35.308	31.293		−66.9	2	-3/2
35.775	31.611		−66.9	2	+1/2
38.048	33.935		−66.9	2	-5/2
38.760	34.382		−66.9	2	-1/2
41.263	37.034		−66.9	2	-7/2
42.318	37.679		−66.9	2	-3/2
42.976	38.160		−66.9	2	+1/2
46.585	41.636		−66.9	2	-5/2
47.653	42.366		−66.9	2	-1/2
51.748	46.435		−66.9	2	-7/2
53.410	47.546	-3×10^{-14}	−66.9	2	-3/2
54.539	48.410		−66.9	2	+1/2
60.577	54.030		−66.9	2	-5/2
62.442	57.590		−66.9	0	-3/2
62.527	55.439		−66.9	2	-1/2
69.687	62.295		−66.9	2	-7/2
72.924	64.609	-3×10^{-11}	−66.9	2	-3/2
75.480	66.582		−66.9	2	+1/2
75.524	69.853		−66.9	0	-3/2
86.780	76.911	-9×10^{-11}	−66.9	2	-5/2
91.630	80.518	-8×10^{-11}	−66.9	2	-1/2
96.326	89.010		−66.9	0	-3/2
105.702	93.892	-1.4×10^{-9}	−66.9	2	-7/2
114.882	100.745	-2×10^{-8}	−66.8	2	-3/2
124.087	107.659	-2×10^{-12}	−66.8	2	+1/2
133.522	122.768	-6×10^{-10}	−66.8	0	-2/2
149.344	131.536	-2×10^{-7}	−66.8	2	-5/2
165.689	146.133	-8×10^{-10}	−66.7	2	-7/2
169.871	149.152	-6×10^{-8}	−66.7	2	-7/2
171.606	148.042	-1.3×10^{-6}	−66.7	2	-1/2
173.035	152.632	-1.0×10^{-6}	−66.7	2	-7/2
176.113	156.289	-9×10^{-7}	−66.7	2	-7/2
176.689	157.129	-1.4×10^{-10}	−66.7	2	-5/2
181.215	160.074	-7×10^{-10}	−66.6	2	-5/2
185.920	163.642	-4×10^{-8}	−66.6	2	-5/2
190.232	167.934	-4×10^{-7}	−66.6	2	-5/2
190.509	170.875	-3×10^{-10}	−66.6	2	-3/2
194.198	172.611	-3×10^{-7}	−66.6	2	-5/2
195.011	173.418	-1.3×10^{-8}	−66.6	2	-3/2
199.611	176.821	-4×10^{-7}	−66.5	2	-3/2
203.797	181.086	-5×10^{-6}	−66.5	2	-3/2
208.400	185.944	-9×10^{-6}	−66.4	2	-3/2
208.407	188.721		−66.4	2	-1/2
208.624	180.762	-5×10^{-5}	−66.4	2	-7/2
212.577	190.265	-9×10^{-9}	−66.2	2	-1/2
212.873	192.186	-9×10^{-4}	−66.4	2	-3/2
215.626	196.709	-2×10^{-5}	−66.4	0	-3/2
217.044	192.995	-7×10^{-7}	−66.4	2	-1/2
221.848	196.981	-6×10^{-6}	−66.3	2	-1/2
226.715	202.190	-8×10^{-5}	−66.2	2	-1/2
232.248	211.942	-5×10^{-9}	−65.8	2	+1/2
232.589	208.400	-7×10^{-4}	−66.0	2	-1/2
236.460	213.627	-5×10^{-9}	−64.9	2	+1/2
237.183	215.961	−0.013	−66.0	2	-1/2
239.858	214.741	-5×10^{-9}	−66.3	2	+1/2
243.371	216.624	-4×10^{-8}	−66.0	2	+1/2
247.638	221.339	-2×10^{-7}	−65.8	2	+1/2
250.777	230.247	-2×10^{-8}	−65.6	0	-3/2
253.115	227.532	-2×10^{-6}	−65.5	2	+1/2
256.464	234.147	-1.1×10^{-6}	−65.3	0	-3/2
257.695	235.275	-2×10^{-5}	−65.2	2	+1/2
262.890	239.549	-4×10^{-5}	−64.7	0	-3/2
265.979	224.767	-9×10^{-5}	−64.3	2	-3/2
270.122	246.441	-1.4×10^{-3}	−63.4	0	-3/2
277.215	254.519	−0.021	−60.7	0	-3/2
285.964	264.340	−0.86	−67.5	0	-3/2
411.372	318.650	-2×10^{-9}	−67.8	2	+1/2
441.876	379.663	−0.002	−67.6	2	-5/2
489.071	466.458		−67.6	2	+1/2
531.217	470.254	−0.055	−67.7	0	-3/2
555.460	531.469		−67.8	2	-1/2
613.799	588.830		−67.7	2	-3/2
661.323	627.835		−67.7	2	+1/2
667.781	642.012		−67.7	2	-5/2
704.205	677.444		−67.7	0	-3/2
718.940	692.463		−67.7	2	-7/2
741.968	706.122		−67.7	2	-1/2
817.559	779.664		−67.7	2	-3/2
890.432	850.612		−67.7	2	-5/2
944.607	902.844		−67.7	0	-3/2
949.117	892.623		−67.7	2	+1/2
961.839	920.113		−67.7	2	-7/2